CrossMark

Investigation on charge density, piezoelectric and ferroelectric properties of $(1-x)Ba(Zr_{0.2}Ti_{0.8})O_3–x(Ba_{0.7}Ca_{0.3})TiO_3$ lead-free piezoceramics

S. Sasikumar[1] · R. Saravanan[1] · S. Saravanakumar[2]

Abstract The lead-free $(1-x)Ba(Zr_{0.2}Ti_{0.8})O_3–x(Ba_{0.7}Ca_{0.3})TiO_3$, (x = 0.4, 0.5 and 0.6) (abbreviated as $(1-x)BZT–xBCT$) ceramics were prepared by solid-state reaction method. X-ray diffraction (XRD) study revealed the perovskite phase of the prepared ceramics at room temperature (RT) for all compositions. The XRD powder profile refinement analysis showed no extra phases and the calculated peak intensities matched well with the observed ones. The charge density distribution studies revealed the chemical bonding nature, qualitative and quantitative features of the distributions of the electrons contributed by the dopant atoms in the unit cell. Scanning electron microscopy images revealed the uniform distribution of powder grains. The elemental compositions of the samples were analyzed by energy dispersive X-ray spectrometer. The optical band gap for all the samples has been estimated to be between 3.15 and 3.07 eV. Enhanced piezoelectric constant, d_{33} = 276 pC/N was obtained for x = 0.5 composition in the morphotropic phase boundary (MPB).

1 Introduction

Piezoelectric materials interconvert mechanical energy into electrical energy and vice versa. They are widely used as sensor, actuators, transformers and in other ferroelectric devices [1, 2]. Over the past few decades, lead zirconate titanate (PZT) ceramics have been widely used as piezoelectric materials, which exhibit good piezoelectricity [1, 2]. However, lead-based PZT materials contain more than 60 wt% of lead oxide, which causes various environmental problems and numerous disease symptoms like headaches, constipation, nausea, anemia, nerve, brain, kidney damage, etc. [3]. Thus, lead-based piezoceramics have already been replaced by lead-free materials to protect our environment. Therefore, lead-free piezoelectrics have attracted considerable attention in recent years and great efforts have been made to develop Pb-free piezoelectric materials [4, 5]. A long-standing issue with Pb-free piezoelectrics has been that they are in general of much lower piezoelectricity compared with PZT materials [6]. Among different lead free systems, barium titanate (BT) based systems exhibit excellent piezoelectric properties [7, 8]. Liu et al. [9] first reported a lead free pseudo binary $x[Ba(Zr_{0.2}Ti_{0.8})O_3]–(1-x)[(Ba_{0.7}Ca_{0.3})TiO_3]/[BZT–BCT]$ ferroelectric morphotropic phase boundary (MPB) system to replace PZT based systems. Recently, high-performance lead-free ceramics $Ba(Zr_{0.2}Ti_{0.8})O_3–x(Ba_{0.7}Ca_{0.3})TiO_3$ have been reported, which show a high piezoelectric coefficient of $d_{33} \sim 620$ pC/N at x = 0.5 [10]. A material whose composition 0.5BZT–0.5BCT lies at the morphotropic phase boundary (MPB) shows good piezoelectric properties. The composition 0.5BZT–0.5BCT, also shows a phase diagram similar to lead-based systems like PZT [11, 12] and PMN-PT [13, 14]. Hence BZT–BCT is presently one of the important candidates for many piezoelectric materials due to its lead free nature with an MPB similar to lead based systems and with superior piezoelectric properties as reported in literature [15, 16].

In the present work, the structural, microstructural, optical, dielectric, ferroelectric and piezoelectric

✉ S. Sasikumar
  sasikuhan@gmail.com

1 Research Centre and Post Graduate Department of Physics, The Madura College, Madurai, Tamil Nadu 625 011, India

2 Department of Physics, Kalasalingam University, Krishnankoil, Virudhunagar, Tamil Nadu 626 126, India

properties of $(1-x)$BZT–xBCT ceramics have been studied. We have focused our research on the electron density distributions and bonding nature of $(1-x)$BZT–xBCT, $x = 0.4$, 0.5 and 0.6 ceramics using maximum entropy method (MEM) [17].

2 Experimental

In this work, $(1-x)$Ba$(Zr_{0.2}Ti_{0.8})O_3$–x$(Ba_{0.7}Ca_{0.3})TiO_3$, $(x = 0.4, 0.5$ and 0.6) ceramics were synthesized by conventional solid-state reaction method. Commercially available powders of $BaCO_3$ (99.99%), $CaCO_3$ (99.95%), TiO_2 (99.99%) and ZrO_2 (99.99%) were used as raw materials. The raw chemicals were mixed with stoichiometric proportions and ball-milled for 12 h. Subsequently, the mixed powders were calcined in alumina crucibles at 1350 °C for 2 h. The calcined powders were ground and 2% polyvinyl alcohol (PVA) was added as binder, pressed into pellets with diameter of 12 mm and thickness of 1 mm. Then, the pellets were sintered at 1450 °C in air for 3 h at heating rate of 5 °C/min.

The phase structure of solid solutions was analyzed using powder X-ray diffraction. The XRD data were recorded using X-ray diffractometer (Bruker D8 Advance) with CuK$_\alpha$ radiation ($\lambda = 1.5406$ Å) in the 2θ range 20°–120° with a scanning step size of 0.02°. The surface morphology of the samples was analyzed by scanning electron microscope (SEM) (Carl Zeiss EVO 18). UV–visible spectrum in the wavelength range from 200 to 2000 nm was recorded using Varian Cary 5000 spectrophotometer. Before measuring the electrical properties, the pellet samples were polished and coated with silver paste on both sides. The dielectric properties were measured using

impedance analyzer (PSM 1735, N4L) in the temperature range from 40–200 °C. All the poling was carried out in silicone oil at 40 °C under a d.c. electric field of 30 kV/cm for 20 min. The polarization–electric field (P–E) hysteresis loops were measured at room temperature using a radiant precision workstation. The piezoelectric constant (d_{33}) values were measured using a d_{33}-meter (SINOCERA, YE2730A).

3 Results and discussion

3.1 Structural analysis

Figure 1 shows the X-ray diffraction profiles of $(1-x)$BZT–xBCT, $(x = 0.4, 0.5$ and 0.6) ceramics recorded at room temperature. The XRD results reveal a pure single phase of perovskite structure without any trace of impurities. The samples of $x = 0.4$ and $x = 0.6$ exhibit tetragonal symmetry with P4mm space group. Splitting of the (200) diffraction peak at 2θ ~ 45° is observed in the sample of $x = 0.5$ as shown in Fig. 1b. This indicates the coexistence of rhombohedral and tetragonal phases (R + T) related to the MPB region. In $(1-x)$BZT–xBCT system, the Ca ions prefer A-sites (Ba-sites) and Zr ions prefer B-sites (Ti-sites) in the perovskite lattice. The XRD peaks shift to higher 2θ angles with increasing x content. This is expected because the ionic radius of Ba^{2+} (1.35 Å) is larger than that of Ca^{2+} (0.99 Å) [18], substituting on A-site. Similar situation exists for Zr^{4+} (0.98 Å) substituting for Ti^{4+} (0.72 Å) [18] on B-site. Similar observations have also been reported by other researchers [19–21]. The crystallite size of the sintered powders has been estimated using Scherrer equation [22] as given in Eq. (1) below,
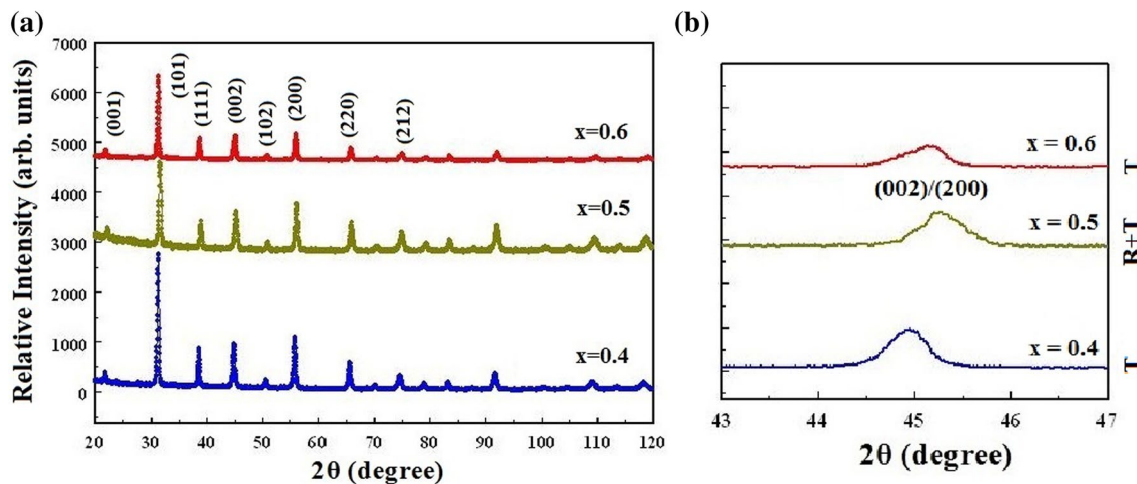

Fig. 1 **a** XRD patterns of $(1-x)$BZT–xBCT, $(x = 0.4, 0.5, 0.6)$ ceramics, **b** expanded X-ray diffraction patterns for (002) peak

$$d = \frac{0.9\lambda}{\beta \cos \theta} \tag{1}$$

where 0.9 is the shape factor, λ is the X-ray wavelength ($\lambda = 1.54056$ Å), β is the line broadening at half the maximum intensity in radians and θ is the Bragg's angle. The estimated average crystallite size of $(1 - x)$BZT–xBCT, ($x = 0.4$, 0.5 and 0.6) ceramic samples are about 27, 18 and 25 nm, respectively.

3.2 Rietveld refinement analysis

The Rietveld refinement [23] of the experimental XRD data of $(1 - x)$BZT–xBCT, ($x = 0.4$, 0.5 and 0.6) ceramic samples was carried using JANA 2006 [24] software. Figure 2a–c show the fitted profiles and difference profiles of $(1 - x)$BZT–xBCT, ($x = 0.4$, 0.5 and 0.6) with corresponding model of tetragonal structures respectively. In Rietveld [23] analysis, the XRD data sets are refined by minimizing the difference between the observed and calculated powder diffraction patterns. In this work, from the refinements, Ba and Ca ions are assumed to share the same crystallographic A-site of the perovskite structure. Similarly, Ti and Zr ions are positioned at B-site. Results of the structural refinement show that the diffraction peaks of $x = 0.4$ and 0.6 can be indexed to tetragonal phase with space group P4mm. Figure 2b shows the mixed phase refinement profile for the MPB composition 0.5BZT–0.5BCT with a predominant tetragonal phase (P4mm) and a weak rhombohedral phase (R3m). Table 1 shows the lattice parameters, reliability indices and goodness of fit obtained after fitting using Rietveld refinement [23].

3.3 Microstructure and energy dispersive X-ray spectra analysis

Figure 3a–c show the SEM micrographs of $(1 - x)$BZT–xBCT, ($x = 0.4$, 0.5 and 0.6) ceramics. The SEM image of $x = 0.4$ shows the rectangular-like grains. When x is increased, the shape of the particle changes with respect to the Ca^{2+} concentration. The average particle size of the prepared samples was found to increase with increase in Ca^{2+} concentration. The energy dispersive X-ray (EDS) spectra of $(1 - x)$BZT–xBCT, $x = 0.4$, 0.5 and 0.6 were recorded to determine the chemical composition of the solid solutions and are presented in Fig. 4a–c. The presence of all elements in these ceramics detected by EDS spectra and the EDS data are listed in Table 2. The EDS results revealed that the observed atomic and weight percentages match well with expected values.
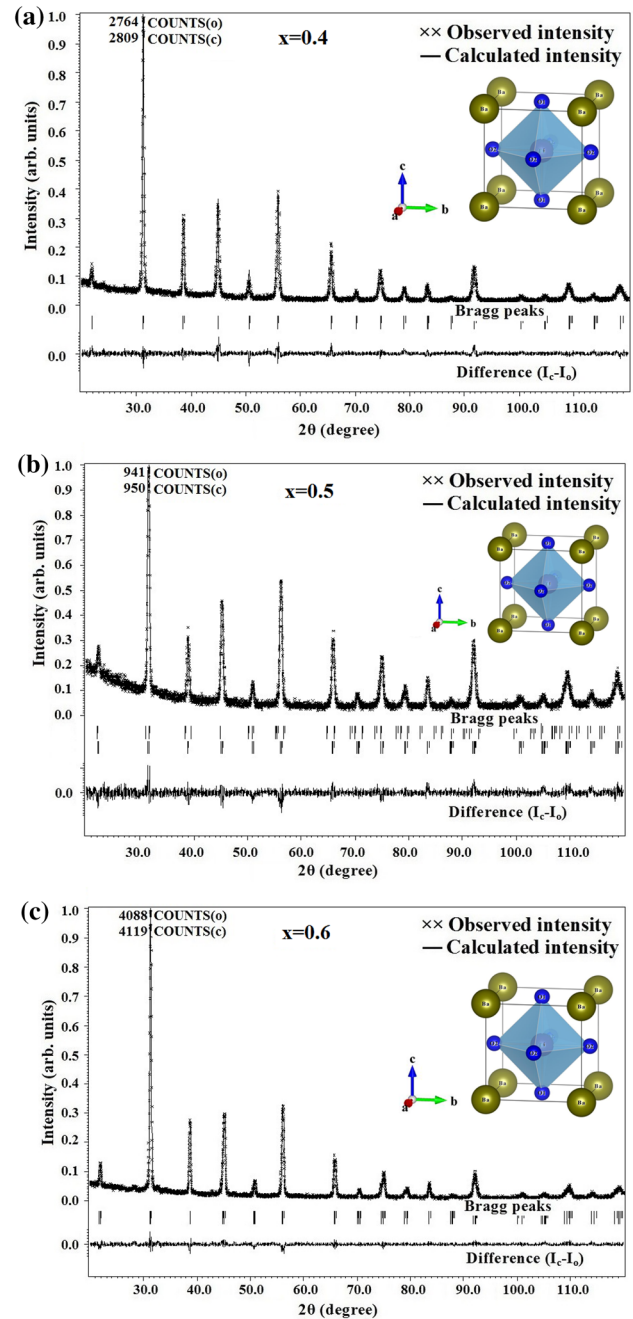

Fig. 2 **a** Fitted powder XRD profile for 0.6BZT–0.4BCT ceramic (inset shows the refined crystal structure). **b** Fitted powder XRD profile for 0.5BZT–0.5BCT ceramic (inset shows the refined crystal structure). **c** Fitted powder XRD profile for 0.4BZT–0.6BCT ceramic (inset shows the refined crystal structure)

3.4 Band gap determination

The optical band gap energy (E_g) was estimated from UV–visible spectral analysis. The optical energy band gap is related

Table 1 Refined parameters of (1−x)BZT–xBCT, (x=0.4, 0.5, 0.6) ceramics through refinement of powder XRD data

Parameters	x=0.4	x=0.5		x=0.6
Phase (Space group)	Tetragonal (*P4mm*)	Tetragonal (*P4mm*)	Rhombohedral (*R3m*)	Tetragonal (*P4mm*)
Lattice parameter (Å)	a=4.0040(1) c=4.0065 (2)	a=4.0141(1) c=3.9945(1)	a=5.4455(2) c=6.6334(3)	a=3.9843(5) c=4.0097(4)
Unit cell volume (Å³)	64.23(3)	64.36(3)	170.16(1)	63.65(1)
Density (gm/cc)	6.02	6.01	6.82	6.08
R_p (%)	8.65	9.99	9.94	7.54
R_{obs} (%)	4.31	5.02	5.28	3.49
GOF	1.24	1.13	1.13	1.17
$F_{(000)}$	102	102	306	102

R_p reliability index for profile, R_{obs} reliability index for observed structure factors, *GOF* goodness of fit, $F_{(000)}$ number of electrons in the unit cell
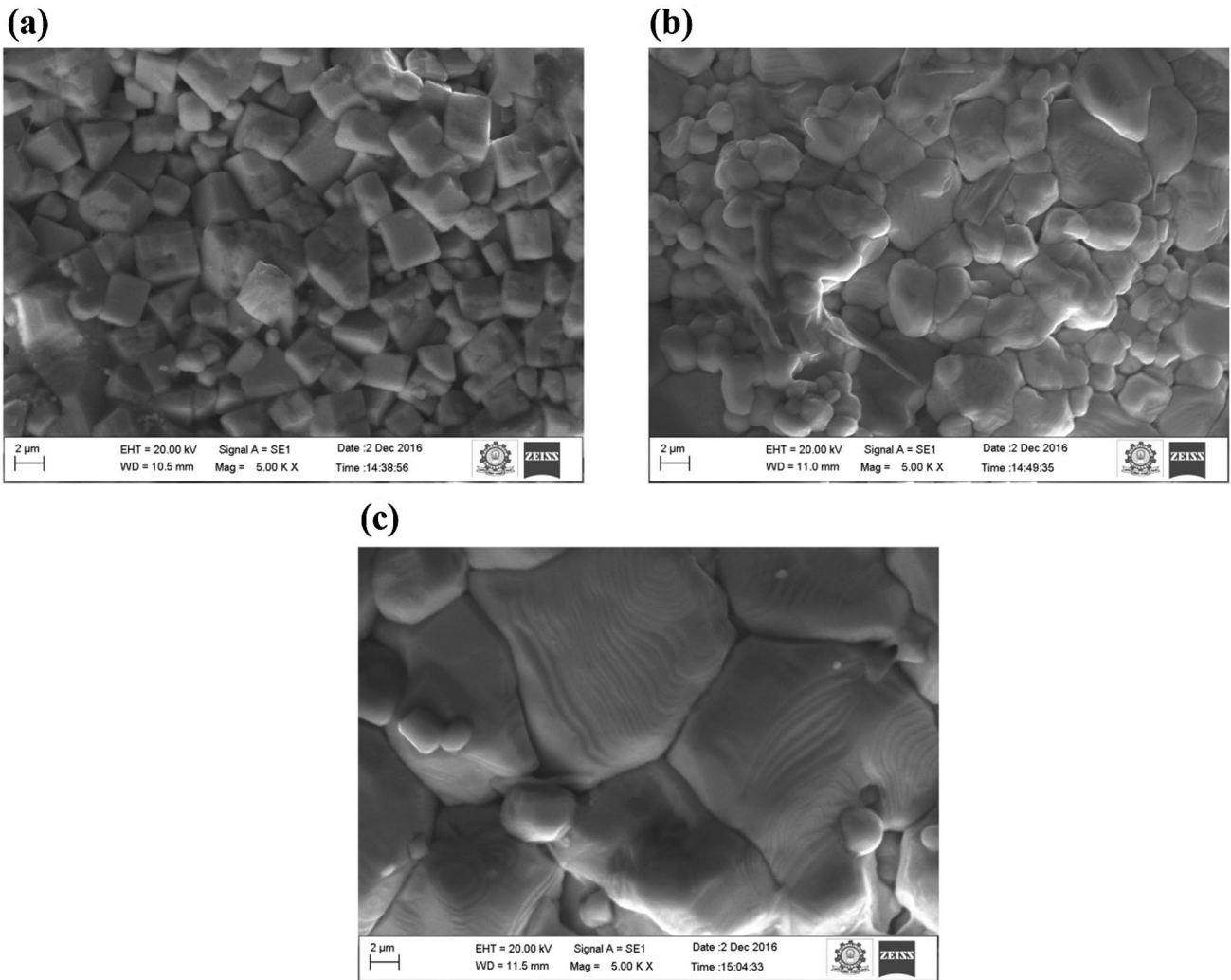

Fig. 3 SEM images of (1−x)BZT–xBCT ceramics with **a** x=0.4, **b** x=0.5 and **c** x=0.6
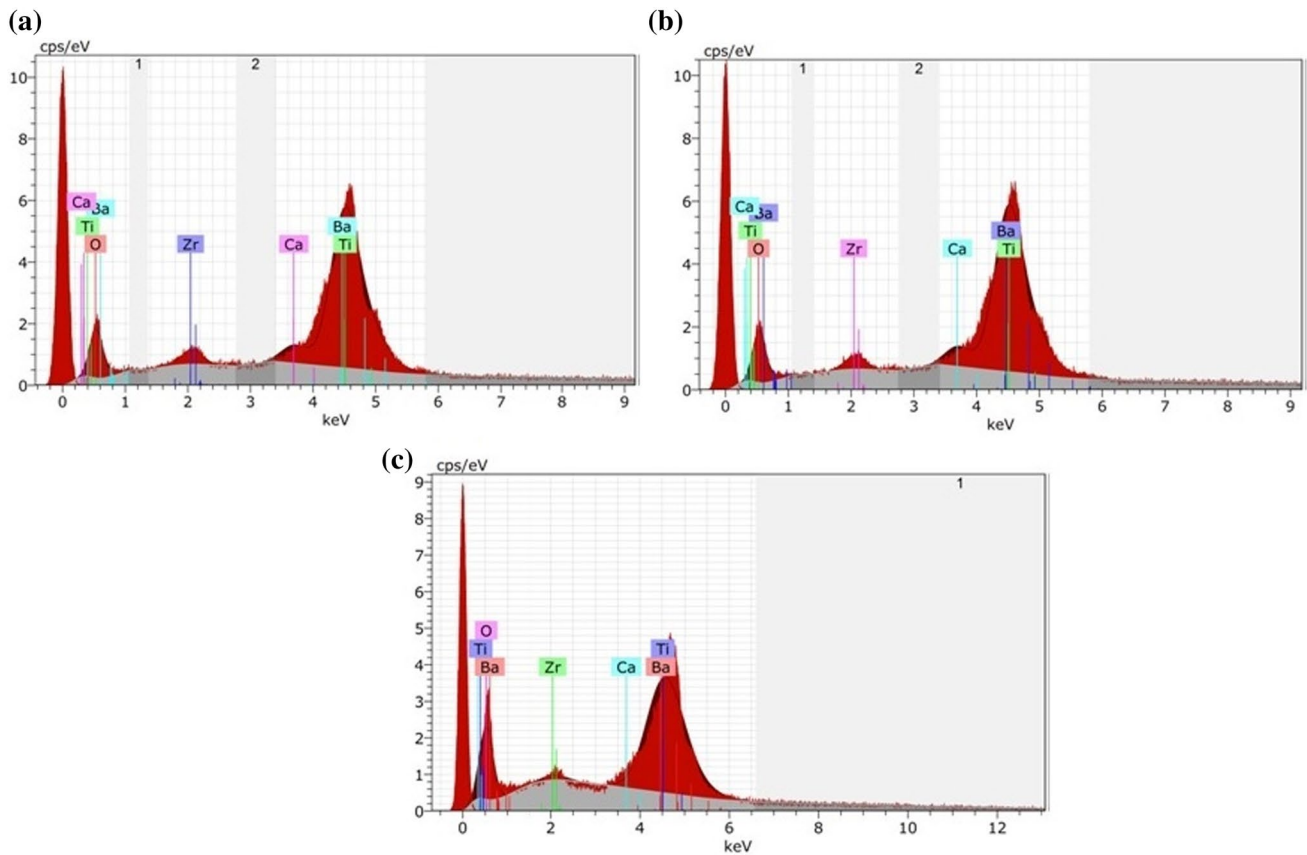
(a)

(b)

(c)

Fig. 4 EDS spectra of $(1 - x)$BZT–xBCT ceramics with **a** x = 0.4, **b** x = 0.5 and **c** x = 0.6

Table 2 EDS elemental composition for $(1 - x)$ BZT–xBCT, (x = 0.4, 0.5, 0.6) ceramics

Samples	Atomic (%)					Weight (%)				
	Ba	Zr	Ca	Ti	O	Ba	Zr	Ca	Ti	O
x = 0.4	4.67	1.59	3.15	22.55	68.04	20.82	4.72	4.10	35.04	35.33
x = 0.5	7.45	1.69	3.32	22.86	65.16	29.83	4.50	3.32	31.94	30.41
x = 0.6	4.63	1.14	3.05	20.27	70.91	21.42	3.52	4.11	32.71	38.24

to absorbance and to the photon energy, which is proposed by following Wood and Tauc [25] equation.

$$(\alpha h\nu)^2 = A(h\nu - E_g) \qquad (2)$$

where A is a proportionality constant, α is the absorbance coefficient, h is the Plank constant, ν is the frequency and E_g is the optical band gap and n is a constant associated with the different types of electronic transitions. It is assigned to a value of 1/2, 2, 3/2 and 3 for direct allowed, indirect allowed, direct forbidden, indirect forbidden transition, respectively.

The usual method of determining the band gap energy is to plot a graph of $(\alpha h\nu)^2$ against energy (hν). The band gap energy (E_g) was determined by extrapolating the straight line portion for the curve to the photon energy axis where $\alpha = 0$ as shown in Fig. 5. The optical band gap values for the $(1 - x)$(BZT)–xBCT, (x = 0.4, 0.5, 0.6) ceramics are determined and listed in Table 3. The band gap values obtained for all the samples range from 3.15 to 3.07 eV, which are slightly less than for reported [26] value, 3.26 eV.
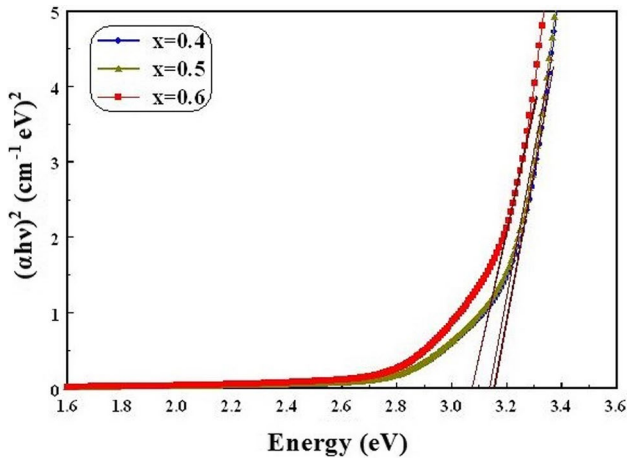
Fig. 5 Tauc plot for $(1-x)$BZT–xBCT ceramics with x = 0.4, 0.5 and 0.6

3.5 Dielectric constant measurements

Temperature dependence of dielectric constant of $(1-x)$ (BZT)–xBCT, (x = 0.4, 0.5, 0.6) ceramics at 10 kHz is shown in Fig. 6. The dielectric constant was measured in the temperature range 40–200 °C. The Curie temperature (T_C) is defined as the temperature that corresponds to the ferroelectric–paraelectric phase transition and the corresponding temperature [27]. In the present work, T_C shifted towards higher temperatures with the increase of x value. 0.5BZT–0.5BCT composition has the highest dielectric constant ($\varepsilon \sim 3702$), due to the presence of mixed structures. The coexistence of rhombohedral and tetragonal phases increases the number of orientations (in polarization) in this composition, which leads to higher dielectric constant. The values of the dielectric constant at 10 kHz for $(1-x)$BZT–xBCT, (x = 0.4, 0.5 and 0.6) ceramics are given in Table 4.

3.6 Ferroelectric and piezoelectric measurements

Figure 7a–c show the room temperature polarization versus electric field plot of $(1-x)$BZT–xBCT, (x = 0.4, 0.5 and 0.6) ceramics measured at an applied field of 4.5 kV/mm. The maximum polarization (P_m), remnant polarization (P_r) and the coercive field (E_C) of the samples are given in Table 4. Figure 7b shows soft P–E loop (x = 0.5) with a maximum polarization (P_m) of 15.12 μC/cm² and a coercivity, $E_C = 3.62$ kV/cm. 0.5BZT–0.5BCT composition exhibits the maximum polarization at room temperature, implying an MPB like behaviour as suggested by XRD patterns.

We measured the piezoelectric constant (d_{33}) of samples poled electrically under an external electric field of

Table 3 UV–visible band gap for $(1-x)$BZT–xBCT ceramics with x = 0.4, 0.5 and 0.6

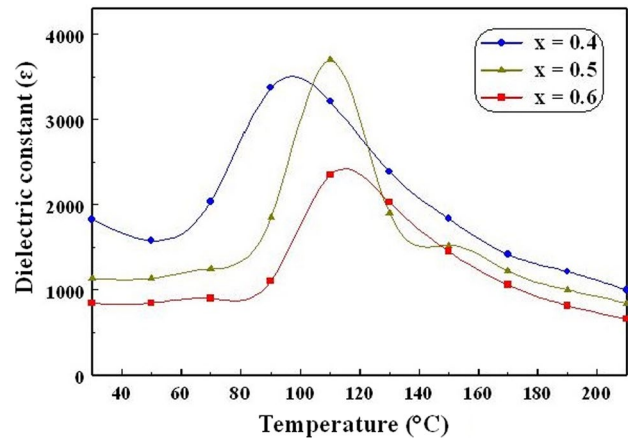| Samples	Band gap values (eV)
x = 0.4	3.15
x = 0.5	3.13
x = 0.6	3.07

Fig. 6 Temperature dependence of dielectric constant (ε) of $(1-x)$ BZT–xBCT ceramics as a function of x

Table 4 Dielectric, ferroelectric and piezoelectric properties of $(1-x)$BZT–xBCT, (x = 0.4, 0.5, 0.6) ceramics

Sample	Dielectric constant[a] (ε)	P_m (μC/cm²)	P_r (μC/cm²)	E_C (kV/cm)	d_{33} (pC/N)
x = 0.4	3374	14.37	5.98	6.02	215
x = 0.5	3702	15.12	4.90	3.62	276
x = 0.6	2151	14.06	5.76	4.88	176

P_m maximum polarization, P_r remnant polarization, E_C coercive field, d_{33} piezoelectric constant

[a](ε) dielectric constant at 10 kHz

30 kV/cm at 40 °C. The improvement on piezoelectric property can be observed in 0.5BZT–0.5BCT ceramics. The d_{33} value is reached maximum at x = 0.5 ($d_{33} = 276$ pC/N) composition, which can be attributed to the coexistence of rhombohedral–tetragonal phases. The presence of mixed phase in the composition x = 0.5 provides favorable condition for easier rotation of the polarization vectors [19, 28]. This makes it evident that the existence of MPB with R + T phases in 0.5BZT–0.5BCT ceramics plays the most important role in improving the piezoelectric properties. Similar results have also been reported
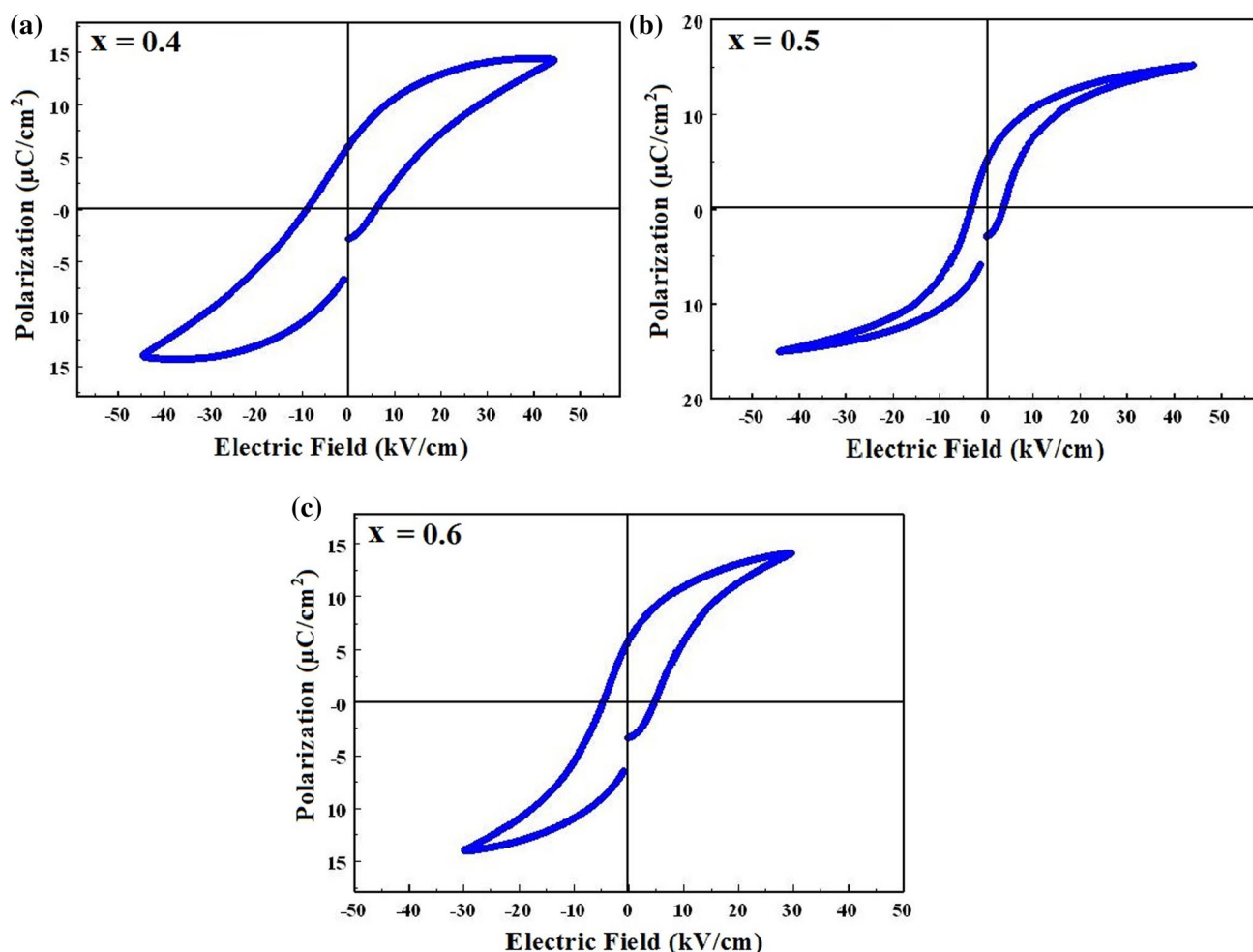
Fig. 7 P–E hysteresis loops for $(1-x)$BZT–xBCT ceramics, **a** x = 0.4, **b** x = 0.5 and **c** x = 0.6 measured at room temperature

in literatures synthesized by solid state reaction method [19, 29].

3.7 Electron density analysis

MEM analysis of X-ray diffraction data is a straightforward approach to derive the interatomic charge density distributions and hence the interaction and bonding characteristics between adjacent atoms. The resultant refined XRD structure factors were used for the construction of charge density in the unit cell using maximum entropy method. Maximum entropy method (MEM) is a standard tool to estimate the accurate charge density which is proposed by Collins (1982) [17, 30, 31]. The charge density distribution was carried out

by considering $64 \times 64 \times 64$ pixels per unit cell. The uniform prior electron density was fixed at each pixel as F_{000}/a_0^3 where F_{000} is the total number of electrons in the unit cell and a_0 is the cell parameter. The estimated charge density distribution in the unit cell was visualized using the software VESTA [32]. Figure 8a–c shows 3D charge density with similar iso-surface level of 1 e/Å^3. Figure 9a shows the 3D unit cell with (0 0 1) plane shaded. Figure 9b–d display the 2D charge density contours in the contour range of 0–1 e/Å^3 with a contour interval of 0.04 e/Å^3 for (0 0 1) lattice plane. It is evident from Fig. 9b–d, that there is no charge overlap between Ba and O which indicates the ionic nature of bonding between Ba and O. Figure 10a shows the 3D unit cell with (0 0 2) plane shaded. Figure 10b–d illustrate the 2D contour maps for (0 0 2)

Fig. 8 Three dimensional electron density isosurfaces for $(1-x)$BZT–xBCT ceramics, **a** $x = 0.4$, **b** $x = 0.5$ and **c** $x = 0.6$
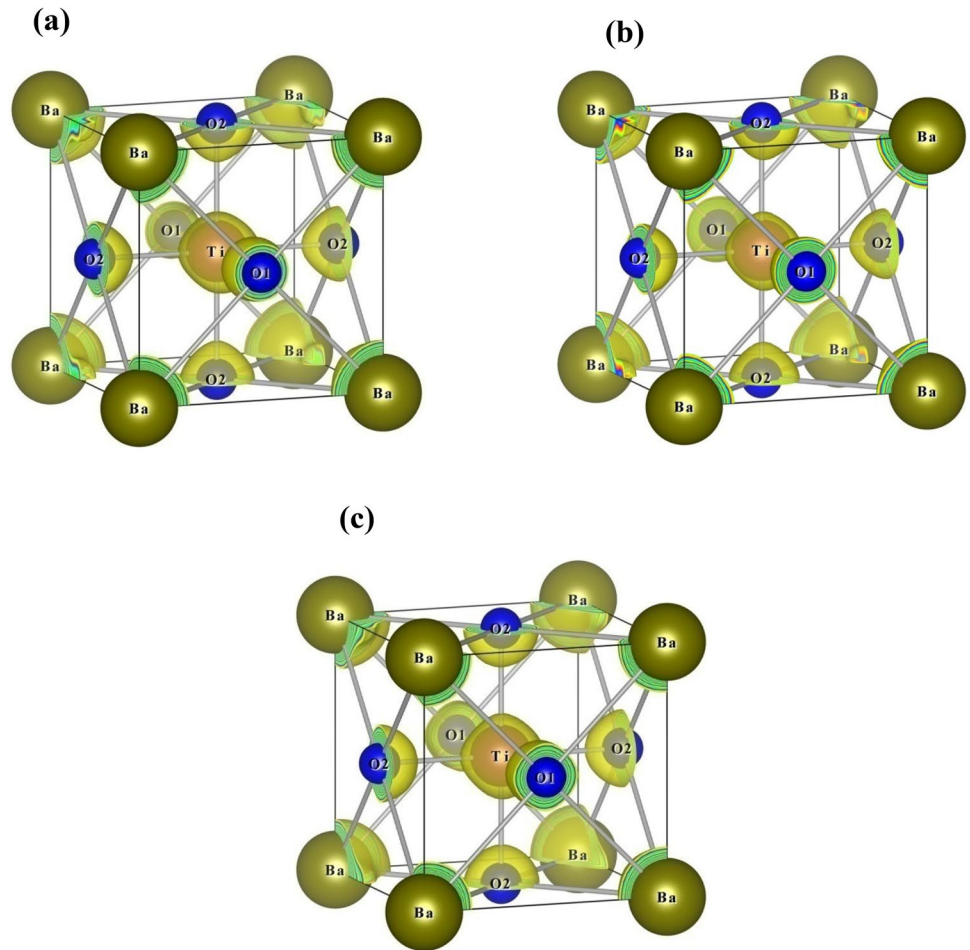
lattice plane representing to the charge density distributions between Ti and O ions. The 2D maps for (0 0 2) lattice plane shows the charge overlap between Ti and O atoms along the bonding region, which confirms the covalent nature of bonding between the Ti and O atoms. Figures 11 and 12 represent the 1D electron density profiles along Ba–O and Ti–O bond respectively. The bond lengths and mid-bond electron density values are given in Table 5.

In titanate perovskite such as $PbTiO_3$ and $BaTiO_3$, the covalent nature of Ti–O bond is primarily responsible for ferroelectric polarization [33]. Table 5 shows mid-bond electron density values for Ba–O bond from 0.1689 to 0.1480 e/$Å^3$, which leads to the ionic behavior between Ba and O ions. Again from Table 5, the electron density

at the middle of the Ti–O bond is found to be 0.9575 e/$Å^3$ for the composition $x = 0.5$. This confirms that the Ti–O bond is covalent in nature. The piezoelectric constant attains a maximum value of $d_{33} \sim 276$ pC/N at $x = 0.5$, corresponding to a relatively maximum polarization of $P_m \sim 15.12$ µC/cm^2 and a relatively low coercive field of $E_C \sim 3.62$ kV/cm. The enhanced piezoelectric and ferroelectric properties can be attributed to the covalent nature of the Ti–O bond.

4 Conclusion

Lead-free $(1-x)Ba(Zr_{0.2}Ti_{0.8})O_3 - x(Ba_{0.7}Ca_{0.3})TiO_3$ $(x = 0.4, 0.5$ and $0.6)$ ceramics were synthesized by

Fig. 9 **a** 3D unit cell of $(1-x)$ BZT–xBCT with (0 0 1) plane shaded. Two dimensional electron density distribution on (0 0 1) plane (along [100] and [010] directions) for $(1-x)$ BZT–xBCT ceramics, **b** x = 0.4, **c** x = 0.5 and **d** x = 0.6
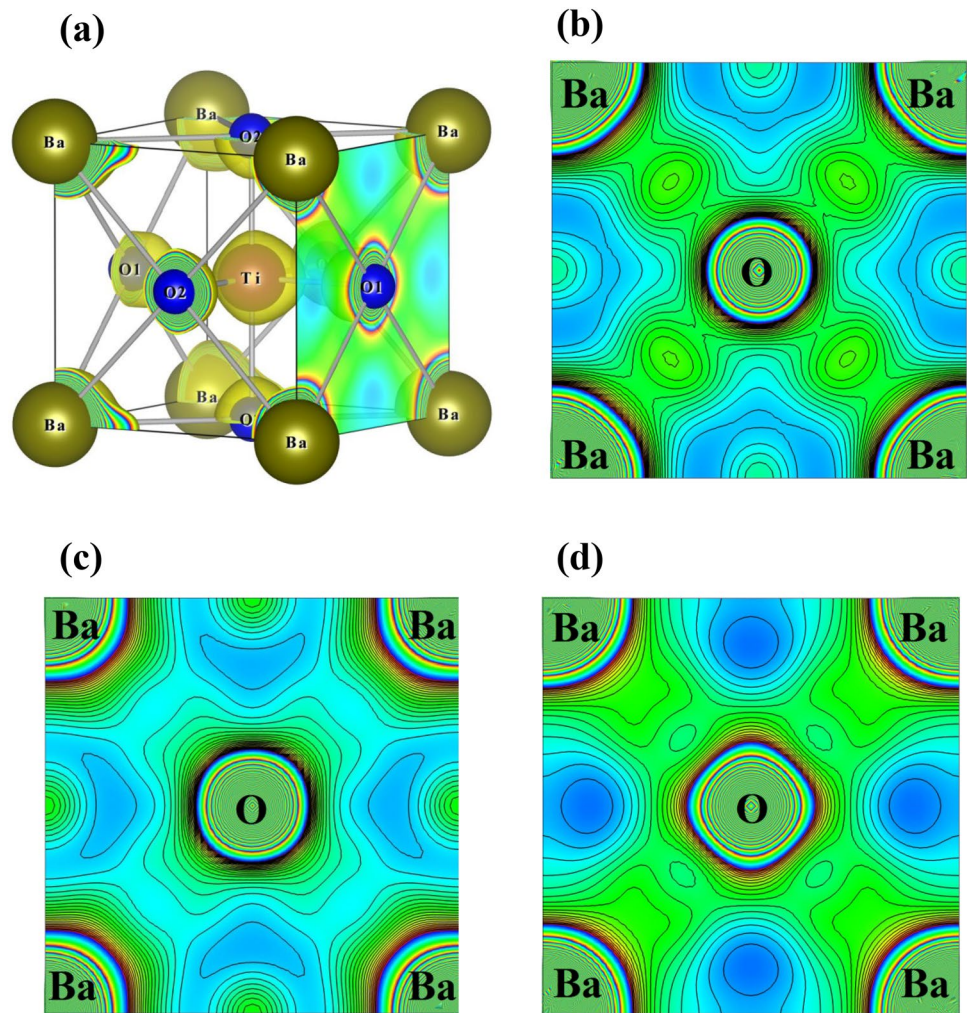
solid-state reaction method. The powder X-ray diffraction revealed combination of rhombohedral and tetragonal phases in 0.5BZT–0.5BCT composition. The microstructures of the synthesized samples were investigated by scanning electron microscopy (SEM). Optical properties investigated by ultraviolet visible (UV–vis) absorption spectroscopy showed a decrease in band gap energy from 3.15 to 3.07 eV. The charge density distribution of $(1-x)$BZT–xBCT ceramics revealed the bonding nature between Ba–O ions and covalent nature between Ti–O obtained from the maximum entropy method. The ferroelectric, piezoelectric and charge derived properties of the composition x = 0.5 have been correlated. 0.5BZT–0.5BCT solid solution showed the highest dielectric constant, $(\varepsilon) = 3702$. The phase transition temperature increases with the increase of x value. The maximum polarization (P_m) and remnant polarization (P_r) observed for 0.5BZT–0.5BCT ceramics are 15.12 and 4.90 $\mu C/cm^2$ respectively. The enhanced piezoelectric and ferroelectric properties of the lead-free ceramic (x = 0.5) can be attributed to the MPB with co-existence of rhombohedral and tetragonal phases.

Fig. 10 **a** 3D unit cell of (1 − x) BZT–xBCT with (0 0 2) plane (along [100] and [010] directions) shaded. Two dimensional electron density distribution on (0 0 2) plane for (1 − x)BZT–xBCT ceramics, **b** x = 0.4, **c** x = 0.5 and **d** x = 0.6
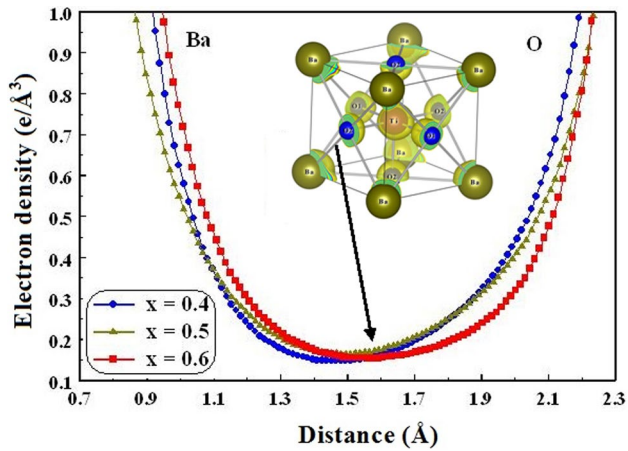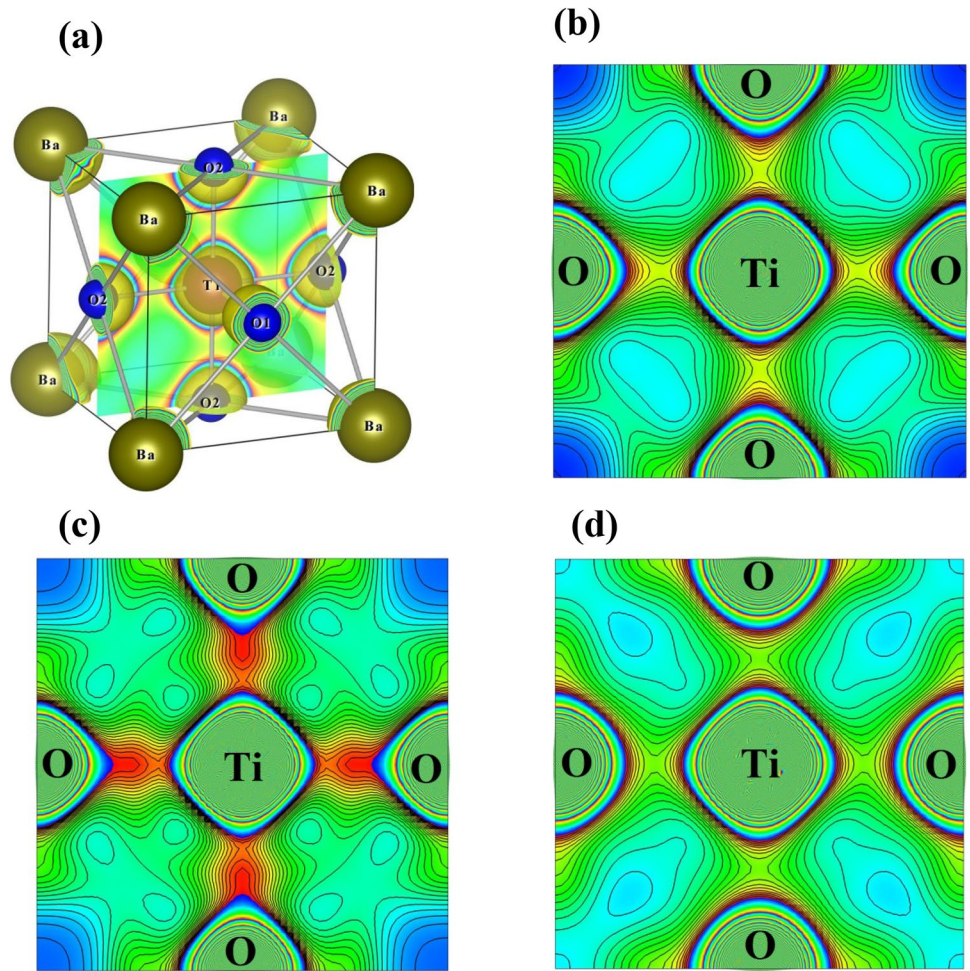
Fig. 11 One dimensional electron density profiles along Ba and O atoms in (1 − x)BZT–xBCT ceramics, (x = 0.4, 0.5, 0.6)
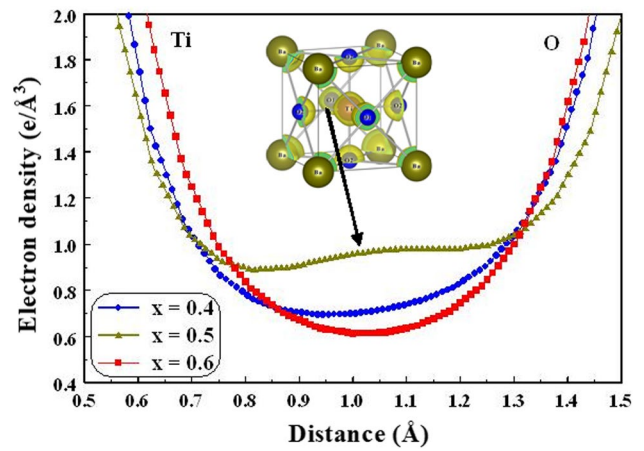
Fig. 12 One dimensional electron density profiles along Ti and O atoms in (1 − x)BZT–xBCT ceramics, (x = 0.4, 0.5, 0.6)

Table 5 Bond lengths and mid-bond electron densities for Ba–O and Ti–O bonds for $(1-x)$BZT–xBCT, $(x = 0.4, 0.5, 0.6)$

Samples	Ba–O		Ti–O	
	Bond length (Å)	Mid-bond electron density (e/Å^3)	Bond length (Å)	Mid-bond electron density (e/Å^3)
x = 0.4	2.8322	0.1681	2.0020	0.6998
x = 0.5	2.8315	0.1689	2.0071	0.9575
x = 0.6	2.8263	0.1480	1.9922	0.6150

References

1. B. Jaffe, W.R. Cook, H.C. Jaffe, *Piezoelectric Ceramics, Chap. 1.* (Academic Press, London, 1971), pp. 1–5
2. G.H. Haertling, Piezoelectric and electro optic ceramics, in *Ceramic Materials for Electronics*, ed. by R.C. Buchanan (Marcel Dekker, New York, 1986), pp. 135–225
3. T. Takenaka, H. Nagat, J. Eur. Ceram. Soc. **25**, 2693 (2005)
4. G.M. Lee, *Agency for Technology and Standards Industry and Energy of the Korean Government, Seminar on EU Product-Related Regulations* (2004) p. 6
5. T.R. Shrout, S.J. Zhang, J. Electroceram. **19**, 111 (2007)
6. Y. Saito, H. Takao, T. Tani, H. Zou, Z.X. Yue, L.T. Li, Nature **432**, 84 (2004)
7. S. Sharma, P. Kumar, P. Palei, Ceram. Int. **38**, 5597 (2012)
8. J.Q. Qi, B.B. Liu, H.Y. Tian, H. Zou, Z.X. Yue, L.T. Li, Solid State Sci. **14**, 1520 (2012)
9. W. Liu, X. Ren, Phys. Rev. Lett. **103**(257602), 1 (2009)
10. H. Bao, C. Zhou, D. Xue, J. Gao, X. Ren, J. Phys. D **43**, 465401 (2010)
11. K. Uchino, *Ferroelectric Devices, Chap. 7.* (Marcel Dekker, New York, 2000)
12. B. Jaffe, *Piezoelectric Ceramics, Chap. 7.* (Academic Press, New York, 1971)
13. O. Noblanc, P. Gaucher, G. Calvarin, J. Appl. Phys. **79**, 4291 (1996)
14. B. Noheda, D.E. Cox, G. Shirane, J. Gao, Z.G. Ye, Phys. Rev. B **66**, 054104 (2002)
15. W. Liu, X. Ren, Phys. Rev. Lett. **103**, 257602 (2009)
16. P. Wang, Y. Li, Y. Lu, J. Eur. Ceram. Soc. **31**, 2005 (2011)
17. D.M. Collins, Nature **298**(5869), 49 (1982)
18. I. Coondoo, N. Panwar, H. Amorın, M. Alguero, A.L. Kholkin, J. Appl. Phys. **113**, 214107 (2013)
19. P. Mishra, P. Sonia, Kumar, Ceram. Int. **40**, 14149 (2014)
20. Z. Yingze, L. Qianru, L. Wenfeng, W. Danyang, RSC Adv. **6**, 14084 (2016)
21. M.C. Ehmke, J. Daniels, J. Glaum, M. Hoffman, J.E. Blendell, K.J. Bowman, J. Appl. Phys. **112**, 114108 (2012)
22. P. Scherrer, Bestimmung der Grösse und der Inneren Struktur von Kolloidteilchen Mittels Röntgenstrahlen. Nachrichten von der Gesellschaft der Wissenschaften, Göttingen, Mathematisch-Physikalische Klasse **2**, 98–100 (1918)
23. H.M. Rietveld, J. Appl. Crystallogr. **2**(**2**), 65 (1969)
24. V. Petricek, M. Dusek, L. Palatinus, Z. Kristallogr. **229**(5), 345–352 (2014)
25. D.L. Wood, J. Tauc, Phys. Rev. B **5**(8), 3144 (1972)
26. J. Rani, K.L. Yadav, S. Prakash, Mater. Res. Bull. **60**, 367 (2014)
27. Z-H Chen, Z-W Li, J-N Ding, J-H Qiu, Y Yang, J. Alloy. Compd. **704**, 193 (2017)
28. S. Shi, R. Zuo, S. Lu, Z. Xu, X. Wang, L. Li, Curr. Appl. Phys. **11**, s120 (2011)
29. P. Mishra, P. Sonia, Kumar, J. Alloy. Compd. **545**, 210 (2012)
30. S. Saravanakumar, S. Sasikumar, S. Israel, G.R. Pradhiba, R. Saravanan, Mater. Sci. Semicond. Process. **17**, 186 (2014)
31. S. Sasikumar, R. Saravanan, S. Saravanakumar, K. Aravinth, J. Mater. Sci. **28**, 9950 (2017)
32. K. Momma, F. Izumi, J. Appl. Crystallogr. **41**, 653 (2008)
33. Y. Kuroiwa, S. Aoyagi, A. Sawada, J. Harada, E. Nishibori, M. Takata, M. Sakata, Phys. Rev. Lett. **87**, 217601 (2001)